Superhard NbB_{2-x} thin films deposited by dc magnetron sputtering

CrossMark

Nils Nedfors [a,*], Olof Tengstrand [b], Jun Lu [b], Per Eklund [b], Per O.Å. Persson [b], Lars Hultman [b], Ulf Jansson [a]

[a] Department of Chemistry, The Ångström Laboratory, Uppsala University, Uppsala SE-751 21, Sweden
[b] Thin Film Physics Division, Department of Physics, Chemistry and Biology (IFM), Linköping University, Linköping SE-581 83, Sweden

ARTICLE INFO

ABSTRACT

We have deposited weakly textured substoichiometric NbB_{2-x} thin films by magnetron sputtering from an NbB_2 target. The films exhibit superhardness (42 ± 4 GPa), previously only observed in overstoichiometric TiB_2 thin films, and explained by a self-organized nanostructuring, where thin TiB_2 columnar grains hinder nucleation and slip of dislocations and a B-rich tissue phase between the grains prevent grain-boundary sliding. The wide homogeneity range for the NbB_2 phase allows a similar ultra-thin B-rich tissue phase to form between thin (5–10 nm) columnar NbB_{2-x} grains also for films with a B/Nb atomic ratio of 1.8, as revealed here by analytical aberration-corrected scanning transmission electron microscopy. Furthermore, a coefficient of friction of 0.16 is measured for an NbB_{2-x} film sliding against stainless steel with a wear rate of 5×10^{-7} mm³/Nm. X-ray photo-electron spectroscopy results suggest that the low friction is due to the formation of a lubricating boric acid film.

© 2014 The Authors. Published by Elsevier B.V. This is an open access article under the CC BY-NC-ND license (http://creativecommons.org/licenses/by-nc-nd/3.0/).

1. Introduction

Transition metal diborides (MeB_2) exhibit a combination of interesting properties, such as high hardness, high wear resistance, high conductivity, and refractory properties. They are generally deposited as thin films using magnetron sputtering with TiB_2 as the most widely studied diboride [1–7], but there are also reports on CrB_2 [8–10], ZrB_2 [11–13], HfB_2 [14,15], WB_2 [16], and TaB_2 [17]. MeB_2 films are almost exclusively sputtered from a compound MeB_2 target since a reactive process is undesirable considering the toxic nature and explosiveness of B-containing gases. The sputtering of a compound MeB_2 target, however, adds complexity to the sputtering process due to the difference in physical properties between B and the transition metal (Me). As a consequence, a wide range of stoichiometries are reported for films sputtered from a MeB_2 target. Mayrhofer et al. report B/Ti ratios of up to 3.2 for films sputtered from a TiB_2 target [3], while Zhou et al. obtain a B/Cr ratio of 0.9 when sputtering from a CrB_2 target [10]. In general, high B/Me ratios have been explained by a longer mean free path for the B atoms within the discharge, resulting in a higher fraction of B atoms in comparison to Me atoms reaching the substrate [1,18]. Low B/Me ratios, on the other hand, are often explained by preferential re-sputtering of the deposited B atoms due to ion bombardment [19].

TiB_2 films deposited by non-reactive dc sputtering frequently exhibit superhard properties (48–77 GPa), which cannot be attributed to prevalent high residual stresses alone [3]. Mayrhofer et al. have studied this effect in more detail and observed that superhardness ($H \geq 40$ GPa) is obtained in overstoichiometric $TiB_{2.4}$ films, while the hardness of stoichiometric bulk TiB_2 is about 25 GPa [3]. The hardening effect was attributed to the self-organized formation of a boron-rich tissue phase along 001-textured TiB_2 columns. The thin TiB_2 columns and the 1- to 2-monolayer-thick tissue phase would impede dislocation motion and nucleation as well as grain boundary sliding and thereby reduce plastic deformation of the material. A recent study by Kalfagiannis et al. has confirmed the importance of overstoichiometric TiB_{2+x} films for superhardness [5]. They also carried out density functional theory (DFT) calculations to demonstrate that a driving force exists to segregate additional boron in the structure to surfaces and interfaces.

The results above suggest that superhard MeB_2 films could only be obtained in overstoichiometric films. However, some diboride phases such as NbB_2 exhibit a wider homogeneity range than TiB_2. The first phase diagram published by Nowotny reported a homogeneity range of 64–76 at.% B (corresponding to $NbB_{1.78}$–$NbB_{3.17}$), whereas a more recent study of Nunes et al. shows a homogeneity range of 65–70 at.% B ($NbB_{1.86}$–$NbB_{2.34}$) [20,21]. This wide homogeneity range suggests that boron can also diffuse to the column boundaries in stoichiometric or even substoichiometric NbB_{2-x} films and thus produce superhard films. However, no studies of magnetron sputtered NbB_2 films have yet been reported to test this hypothesis.

In this study, we investigate the microstructure and mechanical properties of dc magnetron sputtered Nb-B films from a compound NbB_2 target. The films are characterized with a wide range of techniques such as X-ray diffraction (XRD), transmission electron microscopy (TEM), and X-ray photoelectron spectroscopy (XPS). The mechanical and tribological properties are characterized with nanoindentation and ball-on-disc

measurements. We demonstrate that superhard films with a low friction indeed can be obtained in substoichiometric NbB_{2-x} films and that the films exhibit unusually low friction coefficients compared to TiB_2.

2. Experimental details

The NbB_2 films were deposited with non-reactive DC-magnetron sputtering from a 50-mm NbB_2 target (99.5% purity) in an ultra-high vacuum chamber (base pressure of 10^{-7} Pa). XPS depth profiles using rastered 2 keV Ar^+-ion sputtering over an area of 1×1 mm^2 were performed on three different spots on the target surface that was not exposed to the plasma in order to confirm the B/Nb ratio (the XPS equipment is further described below). Sensitivity factors were calculated from Nb-B samples with compositions determined by elastic recoil detection analysis (ERDA). The results showed that the B/Nb ratio in the target was only 1.6. The target was directed towards a rotating substrate holder at a distance of 15 cm and at an angle of 25°. The plasma was ignited in an Ar atmosphere at a constant pressure of 0.4 Pa (3.0 mTorr) and with an Ar gas flow of 45 sccm. The current to the NbB_2-magnetron was kept constant at 150 mA. The samples were coated onto single-crystal Si(001) (10×10 mm^2) and Al_2O_3 (10×10 mm^2) substrates for structure analysis and measurements of mechanical properties and electrical resistivity, Ni-plated bronze (15×15 mm^2) substrates for electrical contact resistance measurements, and mirror-polished 316 L stainless steel (20×20 mm^2) substrates for tribological analysis. The substrates were biased to −50 V and kept at a constant temperature of 300 °C by a heater wire integrated in the substrate holder during deposition. The substrates were preheated for at least 1 h and the targets were pre-sputtered for at least 5 min before deposition. A thin Nb film followed by a thin Nb-C film (total thickness ~50 nm) were deposited onto the substrates prior to the primary deposition in order to improve the adhesion of the thin films to the substrate. These adhesion layers were co-deposited from Nb and C targets (purity 99.95% and 99.999%, respectively) using the same substrate temperature, bias, and process pressure as for the deposition of the NbB_2 films. The current to the Nb magnetron was kept constant at 100 mA and a constant current of 240 mA was applied to the C magnetron during deposition of the NbC layer.

The chemical composition of the thin films was determined by elastic recoil detection analysis (ERDA) using 36 MeV I-ions as the incoming ion beam. The chemical bonding state of the films were measured by XPS using a Physical Systems Quantum 2000 spectrometer with monochromatic Al Kα radiation and an analysis area set to a diameter of 200 μm. Energy calibration was carried out with Au and Ag reference samples. The spectra were acquired after 30 min of Ar^+-ion sputter etching over an area of 1×1 mm^2 with ions having an energy of 200 eV. The B1s spectra of the wear track and the film surface outside the wear track were acquired after 5 min of 200 eV Ar^+-ion sputtering in order to remove surface contaminates adsorbed on the film surface after the tribological test. X-ray diffraction (XRD) measurements were carried out using a Philips X'pert MRD diffractometer with Cu Kα radiation and parallel beam geometry. The grazing incidence XRD (GI-XRD) measurement was performed with a 2° incidence angle. Microscopy studies were carried out on selected films using a Zeiss LEO 1550 scanning electron microscope (SEM) equipped with an AZtec energy-dispersive X-ray spectrometer (EDS) and an FEI Tecnai G2 TF 20 UT field emission gun transmission electron microscope (TEM) operated at a 200-kV acceleration voltage. Scanning TEM (STEM) and electron energy loss spectroscopy (EELS) was performed in the double-corrected Linköping Titan^3 60–300. Spectrum images were collected across the grain-tissue phase interface and the respective spectra subsequently averaged separately. Both cross-sectional and plan view TEM specimens were first mechanically polished to a thickness of ~50 μm, followed by Ar^+-ion milling, with an ion energy of 5 keV. As a final step, the samples were polished using 2 keV Ar^+-ions. Film thicknesses were determined by SEM on fractured cross-sections of the films.

Mechanical properties were obtained using CSM Instruments nano-indenter XP with a diamond Berkovich tip. Load–displacement curves were acquired at 20 different spots on the film surface with an indentation depth set to 50 nm, a loading and unloading rate of 1.5 mN/min. Hardness and elastic modulus values were determined by the Oliver–Pharr method and the presented values are taken as the average from 20 different load–displacement curves [22]. The film adhesion was estimated using a CSEM Scratch Tester equipped with a 200-μm radius Rockwell diamond tip loaded from 0 to 70 N at a loading rate of 100 N/min resulting in a 14-mm scratch path. The critical load of failure is taken at the contact load where an abrupt increase is seen for the acoustic emission. Tribological measurements were performed using a ball-on-disc set-up. Stainless steel balls (100Cr6), intended for ball-bearings and with a radius of 6 mm, were used as the counter surface. The track radius was 2.5 mm, the sliding speed 0.1 m/s, the sliding distance 79 m, and the contact force 1 N. The tribology measurements were carried out in ambient atmosphere with 55% relative humidity. The wear track was investigated by SEM EDS-mapping and optical microscopy using an Olympus AX70 Research Microscope. The wear rate has been calculated from the wear volume, roughly estimated from the surface profile of the wear track investigated using a WYKO NT1100 optical profiler from Veeco. The optical profiler was also used to measure the surface topography and the surface curvature of the film in order to calculate the total residual stress using Stoney's equation corrected for films deposited onto Si(001) substrates [23]. The electrical resistivity was acquired by the four-point probe measurement technique using a CMT-SR2000N from Advanced Instrument Technology. Electrical contact resistance was measured in a custom-built set-up where an Au-coated probe with a 1.65-mm curvature radius is pressed against the film surface. A constant current of 0.1 A is applied and the contact resistance is calculated from the voltage drop over the contact junction. The measurements were performed at nine different spots on the film surface and repeated at two different contact forces of 5 and 10 N. The contact resistance at each contact force was taken as the average value after the two lowest and two highest values had been removed.

3. Results

The lower diffractogram in Fig. 1 shows a typical GI-XRD result from an as-deposited Nb-B film. Diffraction peak positions from a hexagonal AlB_2 structured NbB_2 bulk sample are included in Fig. 1 [24]. As can be seen, all the diffraction peaks can be assigned to hexagonal NbB_2 with lattice parameters $a = 3.12$ Å and $c = 3.28$ Å. As discussed below, this
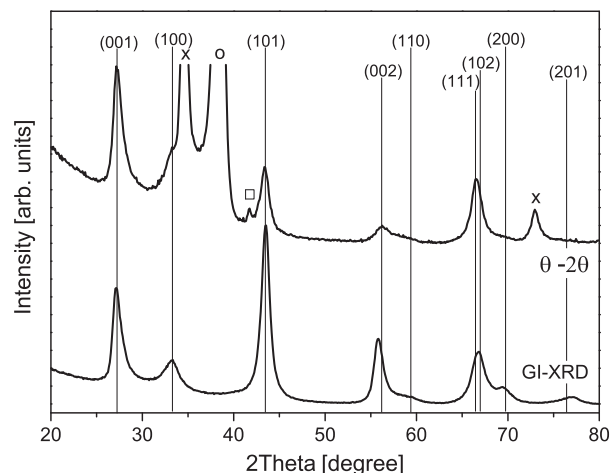

Fig. 1. GI-XRD diffractogram (lower) of the NbB_{2-x} film acquired at an incidence angle of 2°. Upper diffractogram from a θ–2θ scan of the same sample. The peaks marked with × and ○ are assigned to the NbC and Nb adhesion layers, respectively, and the peak marked with □ is assigned to the <001> Al_2O_3 substrate.

is in good agreement with observed values for stoichiometric or substoichiometric NbB$_{2-x}$ bulk samples. The upper diffractogram in Fig. 1 from a θ–2θ scan suggests that the films are weakly textured. In an NbB$_2$ film without texture the I_{001}/I_{101} peak ratio should be about 0.35 [24]. An observed I_{001}/I_{101} peak ratio of 1.9 in Fig. 1 suggests a slight (001) texture and the (001) texture coefficient as defined in ref. [7] is calculated to 2.7. The peaks in the θ–2θ diffractogram that are not seen in the GI-XRD measurement can be assigned to the NbC and Nb adhesion layers as well as the Al$_2$O$_3$ substrate. The relatively high intensity for the adhesion layers can be explained by a strong texture for these layers. As a consequence, a higher amount of lattice planes of these layers are parallel to the film surface compared to the weakly textured Nb-B film resulting in the relatively high intensity.

Fig. 2 shows a fractured cross-sectional SEM image of a typical NbB$_2$ film deposited at 300 °C. As can be seen, the film exhibits a fine-grained columnar microstructure typical for magnetron sputtered boride films [1]. The film in Fig. 2 is about 570 nm thick, which corresponds to a deposition rate of about 2.3 nm/min. The surface roughness of the film deposited onto a Si(001) substrate was measured using an optical profiler and showed a root mean squared value of 7 ± 2 nm. Fig. 3a shows a cross-sectional dark-field TEM image of a typical NbB$_2$ film deposited on Si(001) with thin Nb and NbC bonding layers. The dark-field image, obtained using segments of the 001 and 100 diffraction rings, shows a columnar growth with columns 5–10 nm in width. Fig. 3b is a selected area electron diffraction (SAED) pattern for this film and shows diffraction rings that can be assigned to the hexagonal AlB$_2$ structured NbB$_2$ phase. The SAED pattern confirms that no strong texture exists as consistent with the θ–2θ XRD measurement shown in Fig. 1. In the high-resolution TEM image in Fig. 3c, one column is marked. The image shows a dense structure and elongated NbB$_2$ grains can be seen in the columns.

Fig. 4 contains the results from a plan view STEM-EELS spectrum imaging investigation. The STEM plan view image in (a) shows a two-phase structure with bright grains separated by a dark tissue phase. The pronounced Z-contrast image mechanism enhances the mass difference between grains and tissue phase of the apparent composite and separates Nb from the tissue phase, judging by the significant contrast. The indicated rectangular area in (a) was used for spectrum imaging, and the integrated spectral intensity of the B-K edge, from 190 to 210 eV energy loss is shown in (b) as a B map. Although the spectrum image has been affected by specimen drift during the long acquisition time, the vertically aligned tissue phase component of the indicated area in (a) can be identified as an inclined feature. As can be seen from the map, B is distributed everywhere, signifying that both grain and tissue phase exhibit a B component. Using the spectrum image, the energy loss signal from grains and tissue phase can be averaged separately, as is shown in the graph in Fig. 4. The spectra visualizes the onset of the B-K edge at ~188 eV energy loss, and the onset of the Nb-M edges on top of the B-K edge at 205 eV energy loss. The delocalized nature of the energy loss signal gives an Nb component also in the tissue phase spectrum, although it can be seen that it is lower compared to the
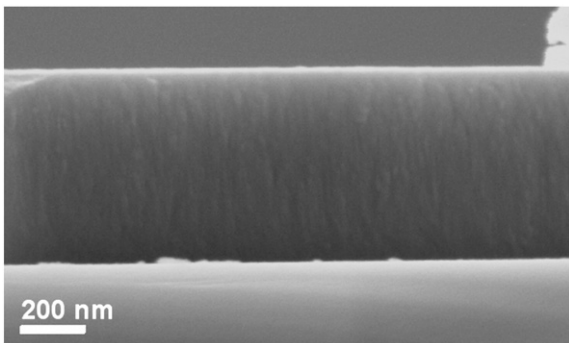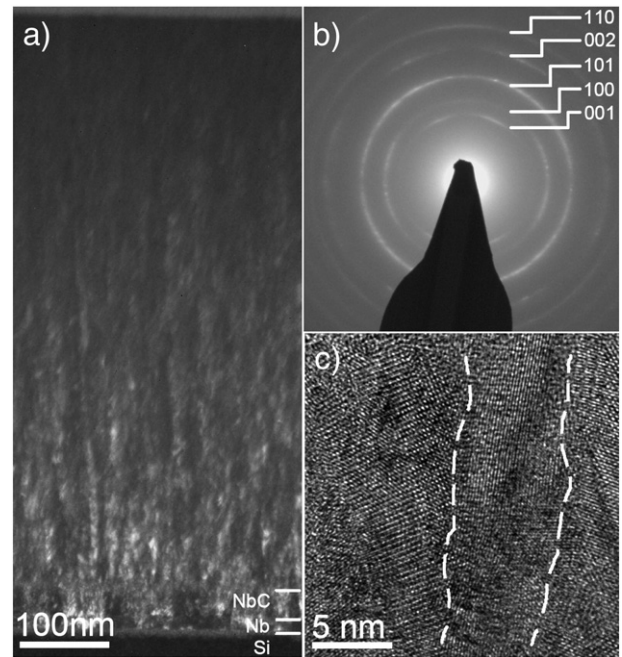

Fig. 3. (a) Dark-field cross-sectional TEM image obtained using segments of the 001 and 100 diffraction rings. (b) SAED pattern of the same film with the diffraction rings indexed to hexagonal NbB$_{2-x}$ with an AlB$_2$ structure. (c) High-resolution cross-sectional TEM image of the same sample with a columnar NbB$_2$ grain marked.

Nb signal from the grain. Viewing the B-K fine structure, a notable difference can be identified, where the grain signal exhibits a single sharp peak, while the tissue phase exhibits two peaks, where the second peak is likely due to delocalization from the grain signal. Due to the thin nature of the tissue phase, delocalization of the EELS signal is present, implying that signals will be mixed for this and similar systems. Anyway, the fine structure differences identify distinctly separate environments for B in tissue phase and grains, respectively.

The chemical composition of the NbB$_2$ films was analyzed with ERDA. The results show a B/Nb ratio of about 1.8, implying a slightly substoichiometric film with a composition NbB$_{-1.8}$. Furthermore, as a consequence of the B tissue phase observed in the STEM EELS investigation, the NbB$_{2-x}$ grains exhibit a B/Nb ratio of <1.8. In the following, these films are denoted as NbB$_{2-x}$. The oxygen and carbon contents in the films were typically less than 1 at% and 2 at%, respectively. The presence of low concentrations of these elements in the NbB$_{2-x}$ films can be attributed to contaminations mainly during transportation of the
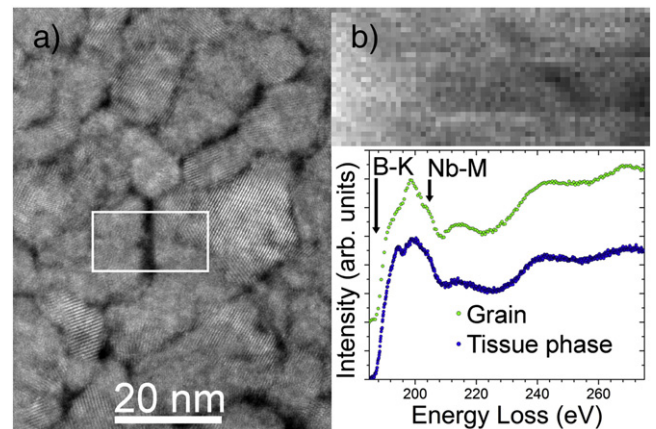

Fig. 4. (a) Plan view STEM image of the NbB$_{2-x}$ film studied in Fig. 3. The indicated rectangular area was used for EELS spectrum imaging. (b) A map over the integrated spectral intensity of the B-K edge, from 190 to 210 eV energy loss. The graph shows the energy loss signal from grains and tissue phase averaged separately.

Fig. 2. Fractured cross-sectional SEM image of an NbB$_{2-x}$ film deposited onto a Si substrate.

samples in air from the deposition chamber to the ERDA analysis. The XPS $Nb3d_{5/2}$ spectrum shows a single peak at 203.6 eV (not shown), which can be assigned to Nb-B bonds in NbB_2 [25]. Fig. 5 shows the XPS B1s spectrum of a typical film after sputter cleaning with Ar^+ ions using a 200-V acceleration voltage for 30 minutes. The spectrum is clearly a combination of several peaks with a main feature at around 188.8 eV. As discussed in Section 4, the B1s peak is most likely a combination of four peaks originating from B in both $NbB_{2−x}$ and boron in B-B bonds.

Nanoindentation measurements of an $NbB_{2−x}$ film deposited onto a Si(001) substrate showed a very high hardness of 42 ± 4 GPa and an elastic modulus of 580 ± 40 GPa. It is known that such high hardness values can be a result of compressive stresses in the film. The residual stress was therefore estimated by applying Stoney's equation on curvature measurements of NbB_2 deposited on a Si(001) wafer. A compressive stress of only 0.9 ± 0.4 GPa was observed. Also, a scratch test was performed in order to evaluate adhesion and critical load of film failure for an $NbB_{2−x}$ film deposited on a stainless steel substrate. The film showed a critical load of 57 N and the scratch path showed that frequent crack formation had occurred, which agrees with the rather small residual stress observed in the films. The crack formation starts already at a load of 6–8 N and the cracks were typically ~200 μm in length. No indication of film delamination was seen, which suggests good film adhesion to the steel substrate.

The friction properties were evaluated by ball-on-disc measurements against stainless steel balls at a relative humidity of 55%. Fig. 6 shows the measured friction curve during 5000 laps (corresponding to a sliding distance of 79 m) for the $NbB_{2−x}$ film. A low and steady coefficient of friction of 0.16 is observed. A second test performed on a different spot on the same sample surface showed an almost identical friction curve. No regions of transferred steel material from the counter steel ball could be seen by SEM or optical microscope investigations of the wear track. However, SEM EDS-mapping (not shown) showed a weak Fe signal homogenously distributed in the wear track. A wear rate of 4 $\times 10^{−7}$ mm^3/Nm was calculated from the volume of the wear track. The transferred steel material will influence the measured wear volume.
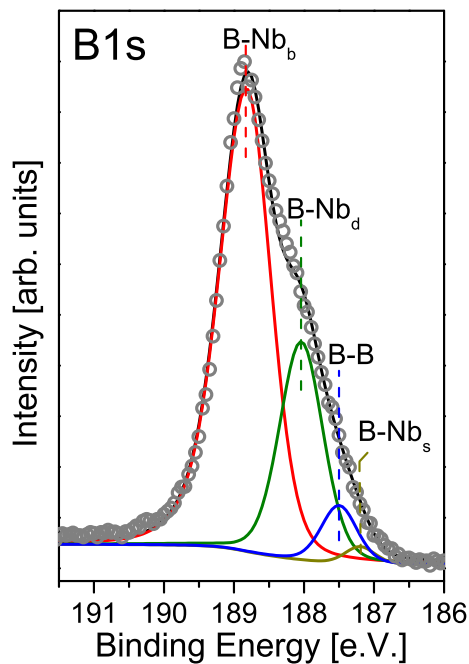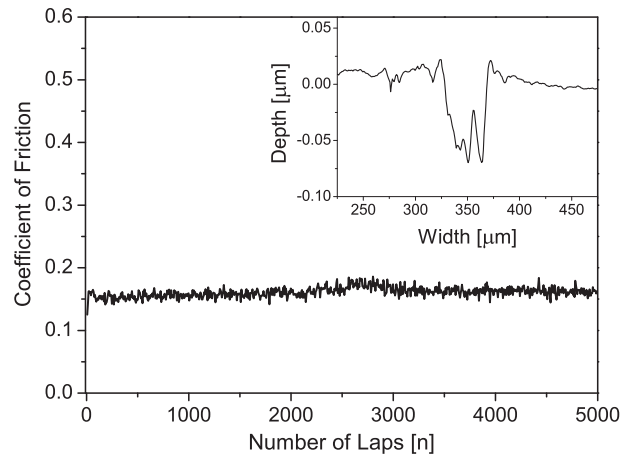

Fig. 6. Measured friction curve for an $NbB_{2−x}$ film when sliding against a stainless steel ball at a relative humidity of 55%. The inset show a profile of the attained wear track.

The volume of transferred material was calculated from the radius of the wear scar on the counter ball and the ball radius. If this volume is added to the volume of the wear track to compensate for the transferred steel material, the wear rate is calculated to be $5 \times 10^{−7}$ mm^3/Nm. A profile of the wear track is shown as an inset in Fig. 6. XPS analysis of the wear track for this film was performed in order to investigate the cause of the low friction (see Fig. 7). A peak appears at 192.8 eV in the spectrum acquired in the wear track. This peak can be assigned to B_2O_3 and agrees with the enhanced oxygen signal seen in the wear track by EDS mapping [26]. A peak at this binding energy can also be due to the presence of boric acid (H_3BO_3) [27], again implying reaction with the ambient.

A resistivity of 100 ± 3 μΩcm was measured for the $NbB_{2−x}$ film using the four-point probe technique. A wide spread in electrical contact resistance was observed between the different spots on the film surface and a drastic reduction in contact resistance from $16,000 \pm 9000$ mΩ to 500 ± 400 mΩ was measured when the contact force were increased from 5 to 10 N.

Fig. 5. XPS B1s spectrum of an $NbB_{2−x}$ film acquired after 30 min of sputtering with 200 eV Ar^+-ions. B-Nb_b, B-Nb_d, and B-Nb_s correspond to B atoms in the bulk, near a defect, and at the surface of the $NbB_{2−x}$ grains, respectively.
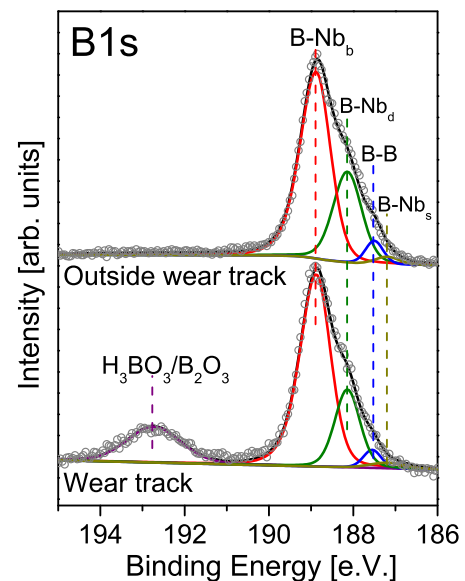

Fig. 7. XPS B1s spectra acquired outside and in the wear track of an $NbB_{2−x}$ film after ball-on-disc measurement against stainless steel. The surfaces were sputtered for 5 min with 200 eV Ar^+-ions prior to the measurement in order to remove surface contaminates adsorbed on the film surface after the tribological test.

4. Discussion

Magnetron sputtering of Nb-B films from an Nb-B target with a B/Nb ratio of 1.6 resulted in films with a B/Nb ratio of about 1.8. Different gas-phase scattering properties between sputtered B and Nb species can probably explain the substoichiometry since a longer mean free path in the Ar-discharge is expected for B [1,18]. As a consequence, a higher amount of B will reach the substrates. The films consist of nanocrystalline NbB_{2-x} grains with a hexagonal AlB_2 structure ($P6/mmm$ space group, number 191) separated by a B tissue phase. The formation of non-stoichiometric films is not surprising considering the wide homogeneity range for the NbB_2 phase in the Nb-B phase diagram. As discussed by Nunes et al., the homogeneity range at thermodynamic equilibrium is most likely about 5 at.%, ranging from $NbB_{1.86}$ to $NbB_{2.34}$ [21]. Magnetron sputtering, however, is carried out far from equilibrium and it is conceivable to assume that compositions outside the equilibrium homogeneity range can easily be obtained during film growth. The B/Nb ratio of about 1.8 observed in our films is therefore not unreasonable. It should be noted that most likely a range of compositions can be obtained for magnetron sputtered NbB_{2-x} films by a careful tuning of the experimental parameters (pressure, substrate/target distance, bias, etc.) or by adding an additional boron source from a second magnetron using an elemental B target. That, however, was not the subject for this study.

Typical lattice parameters for the hexagonal NbB_{2-x} films were $a = 3.12$ Å and $c = 3.28$ Å. A survey of the literature shows a rather large variation in published cell parameter data. This is most likely due to the existence of a homogeneity range, where the cell volume is a function of the B/Nb ratio. Nunes et al. have investigated the effect of composition on cell parameter data on sintered bulk samples and found a clear difference between overstoichiometric NbB_{2+x} and substoichiometric NbB_{2-x} [21]. In boron-deficient samples, they observed $a = 3.112$ Å and $c = 3.263$ Å. For B/Nb > 2, a clear decrease in a-axis to 3.09 Å was observed together with a corresponding increase in c-axis to above 3.31 Å. It is clear that our cell parameter data fits well to B/Nb ratios of <2 in agreement with the chemical analysis discussed above. Nunes et al. also carried out Rietveld refinement of combined X-ray and neutron diffraction data to conclude that samples with a composition of $NbB_{2.33}$ had about 10% vacancies in the Nb positions [21]. No such studies have been published for substoichiometric NbB_{2-x}, but it is likely that vacancies are formed in the boron positions giving rise to defects in the boron sublattice.

The SEM and TEM results shown in Figs. 2 and 3 show a typical columnar growth behavior similar to that observed in magnetron sputtered TiB_2 films (see, e.g. refs. [3,4]). In contrast with Mayrhofer et al., however, we cannot observe a very strong (001) texture [3]. The x-ray diffractogram in Fig. 1 suggests a weak texture with a slightly preferred (001) orientation. The absence of a strong texture is also confirmed by the electron diffraction data. Consequently, our films can be described more as 3D nanocomposites compared to the more 2D-like nanocomposite films in ref [3]. As will be discussed below, this will most likely affect the film's properties. The STEM EELS investigation reveals that the 5- to 10-nm columns are separated by a very thin tissue phase. This phase is shown to contain B, organized in a different chemical environment compared to B in the NbB_{2-x} grains, and is suggested to exist as a few atomic layers of B as in the paper by Mayrhofer et al. [3] The EELS signal in Fig. 4 cannot completely exclude Nb from the tissue phase although it can be concluded that B is the dominant element in the tissue phase. Unlike previous studies [3,5], our films are clearly substoichiometric and the formation of a boron-rich tissue phase will lead to a further reduction of the B/Nb ratio below 1.8 inside the hexagonal NbB_{2-x} grains. It is important to note that a homogeneity range in the phase diagram extending over compositions with B/Me ratios <2 are required for this to be a spontaneous process.

The XPS analysis gives additional information on the chemical bonding in the films. The B1s spectrum in Fig. 5 can clearly be separated into several peaks. A reasonable fit can be obtained with three peaks in accordance to previous XPS on single crystal NbB_2 but a more likely approximation, based on the STEM results, requires an additional peak corresponding to B-B bonds [25,28]. Artifacts caused by sputter damages during the Ar-ion sputter cleaning step can be excluded since an acceleration voltage of only 200 V was used, as described in the experimental section. In a more detailed study of sputter damages during XPS analysis of carbide films by Lewin et al., it has been demonstrated that damage at 200 eV is induced only on highly metastable structures suggesting that no artifacts are present in the spectrum in Fig. 5 [29]. XPS B1s spectra of single-crystalline NbB_2 and ZrB_2 have recently been studied in detailed by Aizawa et al. [25]. They observed that NbB_2 single crystals, in contrast to ZrB_2, exhibit more than one feature in the B1s spectrum, and specifically the three peaks listed in Table 1. The main feature at 188.7 eV was attributed to B bonded to Nb in the bulk of the crystal (B-Nb_b). They also reported a peak at 1.6 eV lower binding energy (187.1 eV), which they attributed to B in the surface layer (B-Nb_s). The peak was explained by a core-level shift caused by different coordination in the surface layer compared to the bulk boron atoms. This core-level shift was not observed in ZrB_2 since the ZrB_2 (001) surface is terminated by Zr atoms. The shift as well as the difference between the two borides could be confirmed with DFT calculations [25]. In addition, Aizawa and coworkers observed a third feature about 0.9 eV below the main peak (187.8 eV). This peak was explained as a "defect peak" of the NbB_2 crystal (B-Nb_d). Although the defect peak was not studied in detail, it is conceivable that it originates from boron atoms close to a boron vacancy in the structure. Based on the data in Table 1, we can now fit our B1s spectrum into three peaks with a main B-Nb_b feature at 188.8 eV, which is 0.1 eV higher in binding energy than the corresponding peak from ref. [25]. This is clearly within the instrumental error. If we assume B-Nb_d and B-Nb_s peaks at 0.8 eV and 1.6 eV below the B-Nb_b peak, respectively, a very good fit is obtained. Furthermore, it can be noted that the B-Nb_d peak in the single crystals studied in ref. [25], has a rather low intensity compared to the main B-Nb_b peak. In our NbB_{2-x} films, however, the area intensity of the defect peak is about 35% of the main feature. This is expected assuming that our substoichiometric films have a higher vacancy concentration than the NbB_2 single crystals used in ref. [25]. The results in the STEM analysis above show the presence of boron in the interface between the diboride grains. If we assume that this tissue phase consists of boron with B-B bonds, we should expect a weak B-B peak in the B1s XPS spectrum. This peak is indeed observed at a position of 187.5 eV, which is in agreement with previously reported binding energy for amorphous B [28].

Nanoindentation studies of the NbB_{2-x} showed a hardness of 42 ± 4 GPa. This is twice as high as the reported hardness for bulk NbB_2 [30]. The high hardness was confirmed by measurements on a different nanoindenter (Hysitron TI-950 Tribo-Indenter) in the Thin Film Physics Division Laboratory in Linköping with a different operator and was then found to be 47 ± 1 GPa (not shown). Thus, it can be concluded that the substoichiometric NbB_{2-x} films are indeed superhard ($H \geq 40$ GPa). Also, the low intrinsic stresses (0.9 GPa) suggest that high hardness is not caused by stresses. Furthermore, in comparison with magnetron-sputtered TiB_2 films, we observed very high hardness in substoichiometric films without a strong texture. It is possible that a further increase in hardness could be obtained with a modification of the process giving a stronger (001) texture, i.e., a more 2D-like nanocomposite structure as the films in ref. [3].

Table 1
A summary of the fitted peaks and their binding energies in the XPS B1s spectrum together with binding energies from reference data. The B-Nb_b, B-Nb_d, and B-Nb_s binding energies are from ref. [25] and the binding energy for B-B is from ref. [31].

Chemical bond	Binding energy (eV)	
	Reference data	This work
B-Nb_b	188.7	188.8
B-Nb_d	187.8	188.0
B-Nb_s	187.1	187.2
B-B	187.5	187.5

Mayrhofer et al. attributed the observed superhardness in overstoichiometric $TiB_{2.4}$ films to the presence of an ultrathin B-rich tissue phase between the TiB_2 columns [3]. The hindering of dislocation nucleation and slip by the nanocolumns in combination with the prevention of grain boundary sliding by the tissue phase result in an enhanced hardness, as reported. The high hardness for our $NbB_{1.8}$ films in comparison to bulk NbB_2 and overstoichiometric $TiB_{2.4}$ films can be explained in a similar way. We observe a dense microstructure consisting of small (5–10 nm) elongated grains separated by a boron-rich tissue phase. The existence of such an interfacial layer should inhibit the nucleation and slip of dislocations and thereby improve the hardness. The elastic modulus of 580 ± 40 GPa for the $NbB_{1.8}$ film is lower compared to bulk NbB_2 with an elastic modulus of 637 GPa [31]. This is a common trend seen for nanocrystalline materials, where the larger fraction of grain boundaries results in a reduced elastic modulus [32].

Typically, diborides from group IV have a rather high friction coefficient against stainless steel. Friction values of 0.5–0.75 have been reported for TiB_2 [4,33]. The observed friction coefficient of 0.16 for the NbB_{2-x} films is therefore surprisingly low considering the high hardness of the film. Erdemir et al. have shown that friction values of 0.05 can be achieved for steel sliding against a VB_2 sample annealed in air. After annealing, a B_2O_3 layer forms on the VB_2 surface, which undergoes a secondary reaction with the moisture in the surrounding air during sliding, resulting in a boric acid lubricating film [34]. The XPS B1s peak at 192.8 eV observed in Fig. 7 shows that B_2O_3 and/or H_3BO_3 (boric acid) has formed in the wear track of the Nb-B film during the tribotest. It cannot be determined to what extent boric acid is present in the wear track due to peak overlap between the B_2O_3 and boric acid peaks. However, the presence of B_2O_3 and presumably boric acid in the wear track of the Nb-B film indicates that the formation of a lubricating boric acid film is causing low friction for this film.

The NbB_{2-x} films exhibited a resistivity of about 100 ± 3 μΩcm, a factor of ten higher than for bulk NbB_2 [35]. The higher resistivity of the magnetron sputtered film can be explained by electron scattering at vacancies and grain boundaries as well as by the poorly conducting B tissue phase separating the boride grains. The high hardness and low friction coefficient combined with a reasonably low resistivity suggest that NbB_{2-x} films may be of interest as electric contact material in sliding contacts, where a low wear rate is required. However, the wide spread and high values in contact resistances observed in this study (≥ 500 mΩ) show that NbB_{2-x} films cannot be directly used in a contact application. Recent studies on sputtered transition metal carbide films have shown that a high hardness will restrict the penetration of the surface oxide and thereby result in a high contact resistance [36,37]. A few monolayers of amorphous carbon in the grain boundaries between the nanocrystalline carbide grains are required to reduce the hardness and increase the toughness. This allows thin oxide layers to break and be penetrated during sliding. Lauridsen et al. has observed promising electrical contact properties for magnetron-sputtered Ti-B-C films consisting of nc-TiC:B grains embedded in an amorphous matrix containing C, BC_x, TiO_x, and BO_x [38]. It is possible that the alloying of carbon to the NbB_{2-x} films can modify the tissue phase leading to a softer and more ductile film with improved contact resistance, as is the subject of a future study.

5. Conclusions

Substoichiometric NbB_{2-x} films with a B/Nb ratio of 1.8 have been sputtered from an Nb-B target (B/Nb ratio 1.6). The films have a dense columnar structure consisting of thin (5–10 nm) NbB_{2-x} grains elongated in the growth direction with a weak 001 texture. It is from STEM and XPS concluded that a B tissue phase one to a few monolayers thick exists in the NbB_{2-x} grain boundaries despite a B/Nb ratio of <2. A measured hardness of 42 ± 4 GPa shows that superhardness can be achieved for weakly textured substoichiometric NbB_{2-x} films. A rather low coefficient of friction, considering a diboride, of 0.16 is measured for the film when sliding against stainless steel. XPS shows the presence of B_2O_3 and presumably boric acid in wear track of the Nb-B film, indicating that the low friction for this film is due to the lubrication from a boric acid film.

References

[1] C. Mitterer, J. Solid State Chem. 133 (1997) 279–291.
[2] O. Knotek, R. Breidenbach, F. Jungblut, F. Löffler, Surf. Coat. Technol. 43–44 (1990) 107–115.
[3] P.H. Mayrhofer, C. Mitterer, J.G. Wen, J.E. Greene, I. Petrov, Appl. Phys. Lett. 86 (2005) 131909.
[4] E. Kelesoglu, C. Mitterer, Surf. Coat. Technol. 98 (1998) 1483–1489.
[5] N. Kalfagiannis, G. Volonakis, L. Tsetseris, S. Logothetidis, J. Phys. D. Appl. Phys. 44 (2011) 385402.
[6] M. Berger, M. Larsson, S. Hogmark, Surf. Coat. Technol. 124 (2000) 253–261.
[7] P. Losbichler, C. Mitterer, Surf. Coat. Technol. 97 (1997) 567–573.
[8] C.H. Cheng, J.W. Lee, L.W. Ho, H.W. Chen, Y.C. Chan, J.G. Duh, Surf. Coat. Technol. 206 (2011) 1711–1719.
[9] M. Audronis, P.J. Kelly, R.D. Arnell, A.V. Valiulis, Surf. Coat. Technol. 200 (2006) 4166–4173.
[10] M. Zhou, M. Nose, Y. Makino, K. Nogi, Thin Solid Films 343–344 (1999) 234–237.
[11] M. Samuelsson, J. Jensen, U. Helmersson, L. Hultman, H. Högberg, Thin Solid Films 526 (2012) 163–167.
[12] R. Khanna, K. Ramani, V. Cracium, R. Singh, S.J. Pearton, F. Ren, I.I. Kravchenko, Appl. Surf. Sci. 253 (2006) 2315–2319.
[13] L. Tengdelius, M. Samuelsson, J. Jensen, J. Lu, L. Hultman, U. Forsberg, E. Janzén, H. Högberg, Thin Solid Films 550 (2014) 285–290.
[14] A.A. Goncharov, S.N. Dub, A.V. Agulov, Phys. Met. Metallogr. 114 (2013) 95–101.
[15] S.N. Dub, A.A. Goncharov, S.S. Ponomarev, V.B. Filippov, G.N. Tolmacheva, A.V. Agulov, J. Superhard Mater. 33 (2011) 151–158.
[16] C.L. Jiang, Z.L. Pei, Y.M. Liu, J.Q. Xiao, J. Gong, C. Sun, Phys. Status Solidi A Appl. Mater. 210 (2013) 1221–1227.
[17] S.T. Lin, C. Lee, J. Electrochem. Soc. 150 (2003) G607–G611.
[18] J. Neidhardt, S. Mráz, J.M. Schneider, E. Strub, W. Bohne, B. Liedke, W. Möller, C. Mitterer, J. Appl. Phys. 104 (2008) 063304.
[19] P. Losbichler, C. Mitterer, W.S.M. Werner, H. Störi, J. Barounig, Thin Solid Films 228 (1993) 56–59.
[20] H. Nowotny, F. Benesovsky, R. Kieffer, Z. Metallkd. 50 (1959) 417–423.
[21] C.A. Nunes, D. Kaczorowski, P. Rogl, M.R. Baldissera, P.A. Suzuki, G.C. Coelho, A. Grytsiv, G. André, F. Boureé, S. Okada, Acta Mater. 53 (2005) 3679–3687.
[22] W.C. Oliver, G.M. Pharr, J. Mater. Res. 7 (1992) 1564–1583.
[23] G.C.A.M. Janssen, M.M. Abdalla, F. van Keulen, B.R. Pujada, B. van Venrooy, Thin Solid Films 517 (2009) 1858–1867.
[24] S.S. Ordanyan, E.E. Nikolaeva, L.V. Kozlovskii, Inorg. Mater. 20 (1984) 1580–1583.
[25] T. Aizawa, S. Suehara, S. Hishita, S. Otani, M. Arai, Phys. Rev. B 71 (2005) 165405.
[26] L. Ramqvist, K. Hamrin, G. Johansson, A. Fahlman, C. Nordling, J. Phys. Chem. Solids 30 (1969) 1835–1847.
[27] J.F. Moulder, W.F. Stickle, P.E. Sobol, K.D. Bomben, Handbook of X-ray Photoelectron Spectroscopy, 3rd ed. Physical Electronics, Inc., Eden Prairie, 1995.
[28] D.N. Hendrickson, J.M. Hollander, W.L. Jolly, Inorg. Chem. 9 (1970) 612–615.
[29] E. Lewin, M. Gorgoi, F. Schäfers, S. Svensson, U. Jansson, Surf. Coat. Technol. 204 (2009) 455–462.
[30] T. Lundström, B. Lönnberg, I. Westman, J. Less Common Met. 96 (1984) 229–235.
[31] W. Matienssen, H. Warlimont (Eds.), Springer Handbook of Condensed Matter and Materials Data, Springer, Berlin, 2005.
[32] A. Cavaleiro, J.M. de Hosson, Nanostructured Coatings, Springer, New York, 2006.
[33] J.T. Ok, I.W. Park, J.J. Moore, M.C. Kang, K.H. Kim, Surf. Coat. Technol. 200 (2005) 1418–1423.
[34] A. Erdemir, M. Halter, G.R. Fenske, Wear 205 (1997) 236–239.
[35] V.A. Gasparov, N.S. Sidorov, I.I. Zver'kova, M.P. Kulakov, J. Exp. Theor. Phys. Lett. 73 (2001) 532–535.
[36] E. Lewin, O. Wilhelmsson, U. Jansson, J. Appl. Phys. 100 (2006) 054303.
[37] N. Nedfors, O. Tengstrand, E. Lewin, A. Furlan, P. Eklund, L. Hultman, U. Jansson, Surf. Coat. Technol. 206 (2011) 354–359.
[38] J. Lauridsen, N. Nedfors, U. Jansson, J. Jensen, P. Eklund, L. Hultman, Appl. Surf. Sci. 258 (2012) 9907–9912.